Spine

SPINE Volume 40, Number 24, pp E1315–E1322

DIAGNOSTICS

A Nondestructive Method to Distinguish the Internal Constituent Architecture of the Intervertebral Discs Using 9.4 Tesla Magnetic Resonance Imaging

Vithanage N. Wijayathunga, PhD,* John P. Ridgway, PhD,† Eileen Ingham, PhD,* Darren Treanor, PhD, FRCPath,‡ Duane Carey, PhD,§ Andy Bulpitt, DPhil,§ Derek Magee, PhD,§ Robin Damion, PhD,¶ and Ruth K. Wilcox, PhD, CEng*

Study Design. An *in vitro* study of the intervertebral disc (IVD) structure using 9.4T magnetic resonance imaging (MRI).

Objective. Investigate the potential of ultrahigh-field strength MRI for higher quality 3-dimensional (3D) volumetric MRI datasets of the IVD to better distinguish structural details.

Summary of Background Data. MRI has the advantages of being nondestructive and 3D in comparison to most techniques used to obtain the structural details of biological tissues, however, its poor image quality at higher resolution is a limiting factor. Ultrahigh-field MRI could improve the imaging of biological tissues but the current understanding of its application for spinal tissue is limited.

Methods. 2 ovine spinal segments (C7–T1, T2–T3) containing the IVD were separately imaged using 2 sequences; 3D spin echo (multislice-multiecho) pulse sequence for the C7–T1 sample and 3D gradient echo (fast-low-angle-shot) pulse sequence for the T2–T3 sample. The C7–T1 sample was subsequently decalcified and imaged again using the same scanning parameters. Histological sections obtained from the decalcified sample were stained followed by digital scanning. Observations from corresponding MRI slices and histological sections were compared as a method of confirmation of morphology captured under MRI. The signal-to-noise ratio (SNR), contrast-to-noise ratio (CNR) and relative-contrast values were calculated for quantitative evaluation of image quality.

Results. Measurements from histology sections and corresponding MRI slices matched well. Both sequences revealed finer details of the IVD structure. Under the spin echo sequence, the annulus lamellae architecture was distinguishable and the SNR and CNR values were higher. The relative contrast was considerably higher between high (nucleus) and low (bone) signal constituents, but between the nucleus and the annulus the relative contrast was low. Under the gradient echo sequence, although the relative contrasts between constituents were poor, the fiber orientation was clearly manifested.

Conclusion. The obtained positive results demonstrate the potential of ultrahigh-field strength MRI to nondestructively capture the IVD structure.

Key words: annulus fibrosus, annulus lamellae, contrast to noise, gradient echo, image quality, intervertebral disc, nucleus pulposus, relative contrast, signal to noise, spin echo, ultrahigh-field MRI.

Level of Evidence: N/A

Spine 2015;40:E1315–E1322

From the *Institute of Medical and Biological Engineering, University of Leeds, Leeds, United Kingdom; †Division of Medical Physics, University of Leeds, Leeds, United Kingdom; ‡The Leeds Institute of Cancer and Pathology, Leeds Teaching Hospitals NHS Trust, St James's University Hospital, Beckett Street, Leeds, United Kingdom; §School of Computing, University of Leeds, Leeds, United Kingdom; and ¶School of Physics and Astronomy, University of Leeds, Leeds, United Kingdom.

Acknowledgment date: March 13, 2015. First revision date: June 29, 2015. Acceptance date: June 29, 2015.

The manuscript submitted does not contain information about medical device(s)/drug(s).

Supported by WELMEC, a Centre of Excellence in Medical Engineering funded by the Wellcome Trust and EPSRC, under grant number WT 088908/Z/09/Z and the European Research Council under the ERC Grant Agreement ERC-2012-StG-306615-BackToBack.

Relevant financial activities outside the submitted work: employment, grants, royalties, patents, stocks, payment for lectures.

Address correspondence and reprint requests to Vithanage N. Wijayathunga, PhD, Institute of Medical and Biological Engineering, School of Mechanical Engineering, University of Leeds, Leeds LS2 9JT, United Kingdom; E-mail: V.N.Wijayathunga@leeds.ac.uk

DOI: 10.1097/BRS.0000000000001075

The intervertebral disc (IVD) plays a crucial role in the biomechanics of the spine, allowing articulation between the vertebrae. Even minor changes in the IVD, whether biological or structural, have the potential to cascade into greater irregularities and significantly affect the biomechanical functions of the spine. Consequently, it is one

of the major sites for back pain, which approximately 70% of the population will experience at some point in their lives.[1]

Detailed information on the substructure of the IVD is usually obtained from histological slices.[2,3] This technique has limitations due to being 2-dimensional (2D) and destructive. 2D micrographs cannot provide accurate height-width-depth as well as spatial orientation details due to sectioning plane alignment and orientation. Hence, there is an element of ''educated guesswork'' involved in understanding such information, which may affect the reliability and consistency of the interpretations. Lack of coherent information along the 3rd direction is particularly disadvantageous when characterizing highly 3-dimensional (3D) structures such as IVDs. For instance, the lamellae in the annulus fibrosus (AF) are curved in their macro state and there exists an alternating fiber pattern in the adjoining lamellae. This fiber orientation is nearly impossible to visualize on a 2D histological section. A 3D method could provide clearer and further information, for example on the morphology of the lamellae within the AF, or the location of annular tears, and could have diagnostic applications if it were nondestructive. Such a technique could also be used preclinically during *in vitro* testing in which different interventions are compared, or for generating accurate computational models of the IVD.

Ultrahigh-field strength magnetic resonance imaging (MRI) systems (4–9.4 T) are an emerging technology for clinical applications. Their capabilities, such as improved signal-to-noise ratio (SNR) and higher spatial resolution, have potential for improved imaging of tissues. The high-field technology has been shown to produce favorable results for imaging of brain tissue, but cardiac and abdominal applications have posed a greater challenge.[4–8] As yet, the use of ultrahigh-field MRI for spinal applications has been relatively limited. Therefore there is a need to examine this imaging methodology for spinal tissue structures, to assess the feasibility of obtaining relevant structural and biological information, as well as identifying suitable imaging protocols.

Visualization of the IVD would benefit from higher resolution due to the multiple structurally distinctive constituents. The hydrated nucleus pulposus (NP) provides a high signal. The AF consists of multiple lamellae and the fiber orientation is completely different in these alternating layers, exhibiting a criss-cross pattern. Consequently, the signal intensity will change depending on the fiber direction. The IVD endplate (EP) also gives rise to different signal intensities due to its cartilaginous and bony components. The aim of this study was to investigate the potential of ultrahigh-field strength MRI to obtain higher quality 3D volumetric MRI data sets of the IVD in order to better distinguish structural details. 2 potentially suitable protocols were investigated and comparisons were made with histological imaging of the same IVD.

MATERIALS AND METHODS

Sample Preparation

2 spines from 5- to 6-year-old sheep (Texel-cross) were obtained from a local abattoir, within 24 hours of slaughter, with veterinary approval. The sheep weighed approximately 40 kg. 2 spinal segments (1 from each spine), containing the C7–T1 and T2–T3 IVD and adjoining vertebrae were separately harvested. Each segment, after securing in a bench grip, was trimmed cranially and caudally by sawing through the vertebral bone close to the vertebral EP. The posterior bony elements were removed close to the posterior margin of the vertebral bodies. The surrounding soft-tissue including the ligamentous structures was also removed. The final trimmed segment was approximately 25 mm in diameter and 20 mm in height. The segments were wrapped in phosphate buffered saline (PBS) soaked paper tissues in order to keep them moist and to avoid drying up during the handling and freezing. PBS was used due to its isotonicity. Subsequently the segments were stored at -20°C.

Prior to MRI scanning, samples were defrosted overnight at 3°C. The sample dimensions were checked during every intermediate step of the process and no measureable changes were found. The samples were positioned in a MRI-safe polymer container with the anterior-posterior direction through the specimen mid-sagittal plane marked on the exposed vertebral bony surface of the specimen. This marked direction was used to align the specimen during mounting to acquire images in the anterior-posterior sagittal or coronal planes of the sample. The containers were sealed with screw-tightened lids during scanning to minimize dehydration.

In view of different possibilities for the change in structural geometry of the sample or loss of material during the decalcification process, a postdecalcification MRI scan was also performed with the same predecalcification scanning parameters in place. The objective was to minimize the geometrical discrepancies between the scanning and the histology procedures.

MR Imaging and Analysis

MR imaging was performed on a 9.4 T scanner having a 89-mm internal diameter vertical bore (AVANCE^{TM} II 400 MHz laboratory NMR system, Bruker, Germany) at a temperature of $22 \pm 0.5^{\circ}$C. The RF coil is 30 mm diameter, birdcage, 1H coil. 3D spin echo (SE) and gradient echo (GE) acquisition techniques were used to achieve high spatial resolution with isotropic voxel dimensions. Given the long acquisition times only 1 pulse sequence was applied to each sample to avoid excessive dehydration of the fresh specimens. The first sample (C7–T1) was imaged using a 3D SE multislice-multiecho pulse sequence (MSME) and the second sample (T2–T3) was imaged using a 3D spoiled GE pulse sequence (Fast Low-Angle Shot—FLASH). The SE and GE-based pulse sequences provide complementary information: the SE pulse sequence was chosen as the use

of multiple 180° RF refocusing pulses minimizes the effect of magnetic field homogeneities induced by the differing magnetic susceptibilities of the different tissue components, therefore resulting an overall higher SNR. The absence of the 180° refocusing pulse in the GE sequence results in signal intensities that are influenced by variations in magnetic susceptibility (known as susceptibility weighted or T2*-weighted contrast). The absence of the 180° RF pulse and the use of a low flip angle excitation pulse allows a much shorter repetition time to be used for the GE pulse sequence in comparison with the SE pulse sequence, enabling a much higher acquisition matrix to be acquired within a comparable acquisition time.

The image acquisition parameters for each pulse sequence are given in Table 1.

Although the SNR is not an absolute measure for quality of biomedical images, it is the most popularly used quantitative method both for assessing the quality of images and for evaluating the effectiveness of image enhancement and signal processing techniques.[9,10] When the magnitude images are calculated from a single set of complex raw data and the spatial distribution of noise is homogeneous, the commonly used technique is based on the signal statistics in 2 separate regions of interest (ROIs) from a single image: 1 in the tissue of interest to determine the signal intensity and 1 in the image background to measure the noise intensity.[10,11] Therefore, this method was selected, using a similar approach to several published studies.[12,13] In order to compare the image quality from the 2 MR sequences, the SNR was measured using image processing software (ImageJ Version1.45 s, NIH). Separate rectangular areas were selected within the AF, NP, and in the vertebral bone respectively. These areas were copied through the image stack, and the consecutive slices were checked to ensure that selected areas were within the corresponding region under consideration. The mean value of the signal intensity for each of these selected areas was calculated. The largest possible rectangular region outside the IVD in the image background (air) was also selected, and the standard deviation of the background noise intensity was calculated. The SNR for each of the areas was then determined by dividing its mean signal intensity by the standard deviation of the background noise intensity.

The contrast-to-noise ratio (CNR) was calculated as $CNR_{a,b} = (S_a - S_b)/SD$ background noise where S denotes signal intensity, "SD" denotes standard deviation, subscripts a and b denote corresponding tissue constituents. The relative contrast (ReCon) was calculated as $ReConab = [(S_a - S_b)/(S_a + S_b)] \times 100$.

For each sample, 5 different images were randomly chosen for SNR, CNR, and relative contrast measurements. The mean value based on the values of the 5 images was finally obtained.

Comparison MR Image Stack with Histology

After the initial scanning, the C7–T1 sample was fixed in 10% (v/v) neutral buffered formalin. It was then transferred to 100 mL ethylenediaminetetraacetic acid (EDTA) of pH 7.0 to 7.4, for decalcification.[14] The sample was continuously shaken and the EDTA solution was replaced daily for a period of 7 days, and subsequently every week for a minimum of 16 weeks. The specimen was imaged using microcomputed tomography (Scanco, microCT100, Switzerland) with a hydroxyapatite phantom for bone mineral density calibration to confirm that complete decalcification had been achieved.

Because there was potential for changes in the structural geometry of the sample or loss of material during the decalcification process, a postdecalcification MRI scan was also performed using the same scanning parameters (except the number of averages). The objective was to minimize the geometrical discrepancies between the scanning and the histology procedures.

TABLE 1. Acquisition Parameters for the 9.4T Images

Scan Parameter	Gradient Echo(FLASH) Sequence	Spin Echo (MSME) Sequence (Before Decalcification)	Spin Echo (MSME) Sequence (After Decalcification)
Repetition time TR (ms)	18.9	1150	1150
Echo time TE (ms)	7.9	14	14
Flip angle	30	180	180
Averages	12	3	4
Pixel bandwidth	97.6562	192.3076923	192.3076923
Echo train length	1	1	1
Width × height × depth (mm)	30.0 × 30.0 × 30.0	29.0 × 29.64 × 29.0	29.0 × 29.7 × 29.0
Acquisition matrix (rows × columns)	512 × 512	260 × 256	260 × 256
Slice thickness (mm)	0.059	0.113	0.113
Number of slices	512	256	256
Acquisition time	16 h 31 min	62 h 48 min	83 h 44 min
Resolution (pixels per mm)	17.067	x- 8.828, y- 8.772	x- 8.828, y- 8.754
Voxel size (mm)	0.059 × 0.059 × 0.059	0.113 × 0.114 × 0.113	0.113 × 0.114 × 0.113

The specimen was then sectioned into 2 halves through the marked mid anterior-posterior line. The resulting right and left halves of the sample were processed and embedded separately in paraffin wax. Using a Leica RM2255 microtome (Leica Microsystems, Milton Keynes UK) 5 μm sections were obtained parallel to the anterior-posterior direction such that their orientation was the same as the imaging plane of the MRI. A selection of sections were stained with haematoxylin & eosin (H&E) and scanned using a slide scanner (Aperio AT2 -Leica Microsystems, Milton Keynes UK)) with a 20 × objective lens. The digital micrographs were sequentially arranged so that the complete stack represented images from the right lateral margin through to the left lateral margin of the sample.

From the postdecalcification MR image stack which consisted of sequential sagittal images between the right and left lateral margins of the specimen, the images representing the sagittal section of the sample at 0.2, 0.4, 0.6, and 0.8 proportional distances between the right and left lateral margins were selected. These were then compared with similarly selected histological micrographs using landmark features and quantitative measurements. (Figures 1–3)

RESULTS

The SNR and CNR values obtained in order to quantitatively compare the images between the different sequences and under different conditions are given in Tables 2 and 3. In all scans, the nucleus produced the best signal. Therefore, ReCon values were calculated in relation to the signal intensity of the nucleus, and are shown in Table 4. The SNR values obtained with SE imaging were higher than those for GE images. It was also evident that when comparing the pre- and postdecalcification images, whereas the SNR values for the postdecalcification images were better, the relative contrast remained largely unchanged except for the vertebral bone marrow (Figure 4A, B). This was likely to be due to the tissue hydration taking place during the decalcification process. The relative contrast between different constituents under GE was relatively poor.

The GE images across the anterior AF of the T2–T3 IVD showed the highly organized AF structure comprising of collagen fibers oriented at alternating directions with successive layers. (Figure 4C, D) The angle between these alternating fiber directions was measured in ImageJ software by drawing line segments parallel to the fiber directions. As shown in Figure 5, this angle was found to be 59°. The MRI-histology comparison is presented in Table 5 for confirmation of the features seen on the MR images.

DISCUSSION

Anatomically, the IVD exhibits 3D structural characteristics. Using 2D projection imaging to study these characteristics is not only challenging but can lead to erroneous interpretations. Recent advances in MRI hardware, software and pulse sequence design have provided the capacity to acquire 3D volumetric MRI scans of the human spine with nearly isotropic resolution under 0.5 mm^3 (*e.g.*, 3D FSE), compared with traditional 2D scans acquired with interslice gaps of around 3 mm. Automatic segmentation algorithms have been developed[9] that extract detailed 3D representations of the IVDs from volumetric MRI. The introduction of phased array coil technology with an increased number of coil elements,[15] and increased field strength, both of which increase the baseline SNR, are particularly important for studies that are notoriously

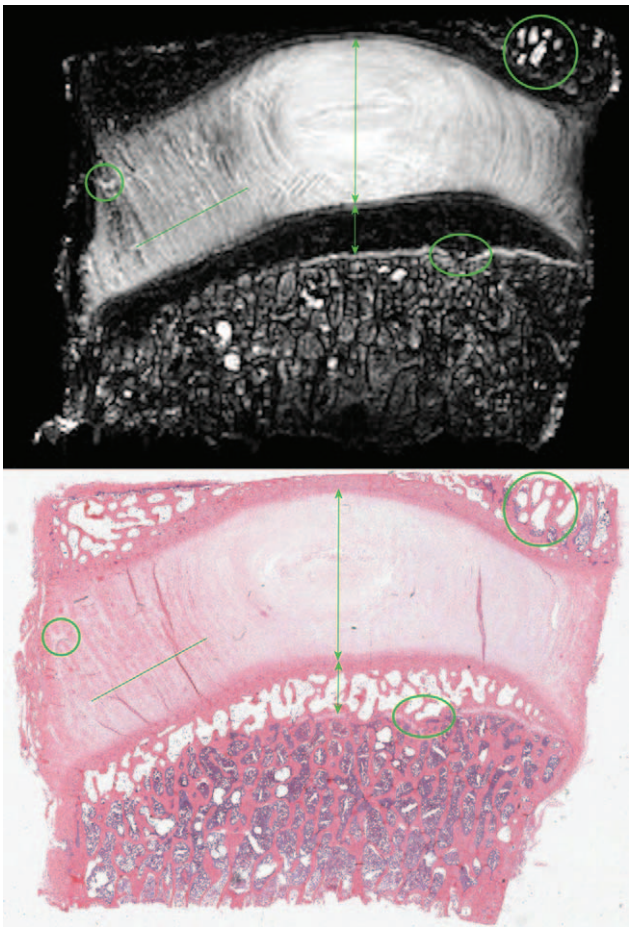

Figure 1. A selected MRI slice from the postdecalcification scan of the C7–T1 IVD and the corresponding histology micrograph. In both images the circles indicate comparative landmarks, vertical arrows indicate height measurements, and the line across the annulus is for lamellae counting.

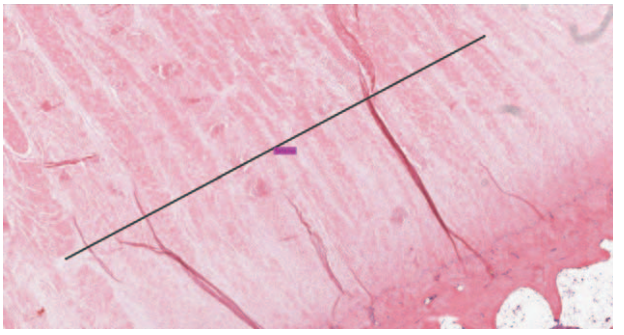

Figure 2. Magnified image of the region in the histology micrograph in FIGURE 1, showing the line drawn across the annulus on the virtual slide for lamellae counting.

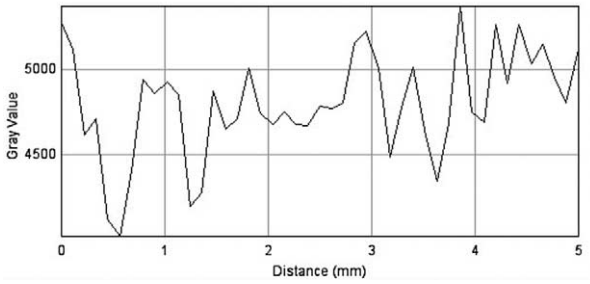

Figure 3. Greyscale variation plot along the corresponding line drawn across the annulus on the MR image for lamellae counting.

SNR deprived, for example, in the AF region of the IVD. Even though ultrahigh-field strength MR scanners are not yet common in the current clinical setting, there is an upward trend in terms of field strength, allowing higher resolution imaging as well as an increased SNR for the acquired images. This opens up the possibility of capturing structural details that previously had not been possible to distinguish *in vivo*. In addition, small bore ultrahigh-field strength MRI scanners are increasingly being used in laboratory settings for *in vitro* studies. The aim of this study was to examine the potential of ultrahigh-field MRI to visualize the substructure of the IVD. In order to confirm the details captured, histology of the same sample was carried out in a manner which allowed the comparison of selected MRI slices with corresponding histological sections.

2 MRI pulse sequences were used in this study: GE and SE. Each method has its own advantages as well as disadvantages. For instance, a GE sequence allows faster image acquisition, and is more sensitive to magnetic susceptibility effects compared with SE, however in general SE provides better SNR for the images.

The SNR derived from the acquired images was higher for the SE sequence. This was partly a consequence of the larger voxel size chosen for this sequence. However, the GE (FLASH) sequence, helped by the higher spatial resolution, revealed more information about the IVD constituents. Collagen present in the IVD is generally difficult to image with MRI, hence the use of gadolinium chelates and magic-angle imaging[16] have been suggested to improve visualization. This study indicates how ultrahigh resolution imaging can provide useful structural information of the collagen-rich IVD.

The consistently higher SNR values obtained for the respective regions after decalcification (Table 2) clearly

TABLE 2. SNR Values Obtained for the Different MR Sequences Performed at Selected Conditions of the 2 Specimens

Sample	Structure/Location	Mean SNR (±SD)
T2–T3(fresh) - GE (FLASH) sequence	Nucleus	12.5 (±0.2)
	Annulus	12.7 (±0.4)
	Vertebral bone marrow	9.0 (±0.5)
C7–T1 (fresh) - SE (MSME) sequence	Nucleus	117.7 (±2.2)
	Annulus	88.3 (±1.1)
	Vertebral bone marrow	12.3 (±5.2)
C7–T1 (postdecalcification) - SE (MSME) sequence	Nucleus	235.9 (±2.2)
	Annulus	180.7 (±2.6)
	Vertebral bone marrow	80.5 (±5.9)

The signal and the noise parameter measurements were based on pixel grey values (intensity).

TABLE 3. CNR Values Obtained for the Different MR Sequences Performed at Selected Conditions of the 2 Specimens. The Signal and the Noise Parameter Measurements Were Based on Pixel Grey Values (Intensity)

Sample	Structure/Location	Mean CNR (±SD)
T2–T3 - GE (FLASH) sequence	Nucleus—bony endplate	Bony endplate was too narrow to select a region
	Nucleus—annulus	−0.2 (±0.3)
	Nucleus—vertebral bone marrow	3.4 (±0.6)
C7–T1 (predecalcification) - SE (MSME) sequence	Nucleus—bony endplate	105.6 (±2.3)
	Nucleus—annulus	29.4 (±3.0)
	Nucleus—vertebral bone marrow	105.4 (±7.0)
C7–T1 (postdecalcification) - SE (MSME) sequence	Nucleus—bony endplate	212.9 (±1.2)
	Nucleus—annulus	55.1 (±2.8)
	Nucleus—vertebral bone marrow	155.4 (±5.6)

TABLE 4. Relative Contrast Values Obtained for the Different MR Sequences Performed at Selected Conditions of the 2 Specimens. The Signal and the Noise Parameter Measurements Were Based on Pixel Grey Values (Intensity)

Sample	Structure/Location	ReCon (±SD)
T2–T3 GE (FLASH) sequence	Nucleus—bony endplate	Bony endplate was too narrow to select a region
	Nucleus—annulus	−0.5 (±1.1)
	Nucleus—vertebral bone marrow	15.8 (±2.9)
C7–T1 (predecalcification)—SE (MSME) sequence	Nucleus—bony endplate	81.7 (±5.7)
	Nucleus—annulus	14.3 (±1.4)
	Nucleus—vertebral bone marrow	81.3 (±7.3)
C7–T1 (postdecalcification)—SE (MSME) sequence	Nucleus—bony endplate	82.3 (±0.6)
	Nucleus—annulus	13.2 (±0.7)
	Nucleus—vertebral bone marrow	49.7 (±2.7)

suggested that tissue hydration had taken place across the entire sample. However, importantly, when ReCon values were considered (Table 4), the relative contrast between different regions remained relatively the same except with the vertebral bone marrow where ReCon was reduced by nearly 40% from the predecalcification value. This indicated that the hydration during decalcification was relatively similar across the disc, but substantially higher when the vertebral bone marrow regions were under consideration. Understandably the bone trabecular structure has the capacity to accommodate more water. Because the hydration was similar across the disc, it was not an issue for consistent visualization of structural details of the IVD.

The MRI-histology comparison confirmed that the features seen on the MR images were realistically related to the actual structures (Figure 1). It was evident from the histology

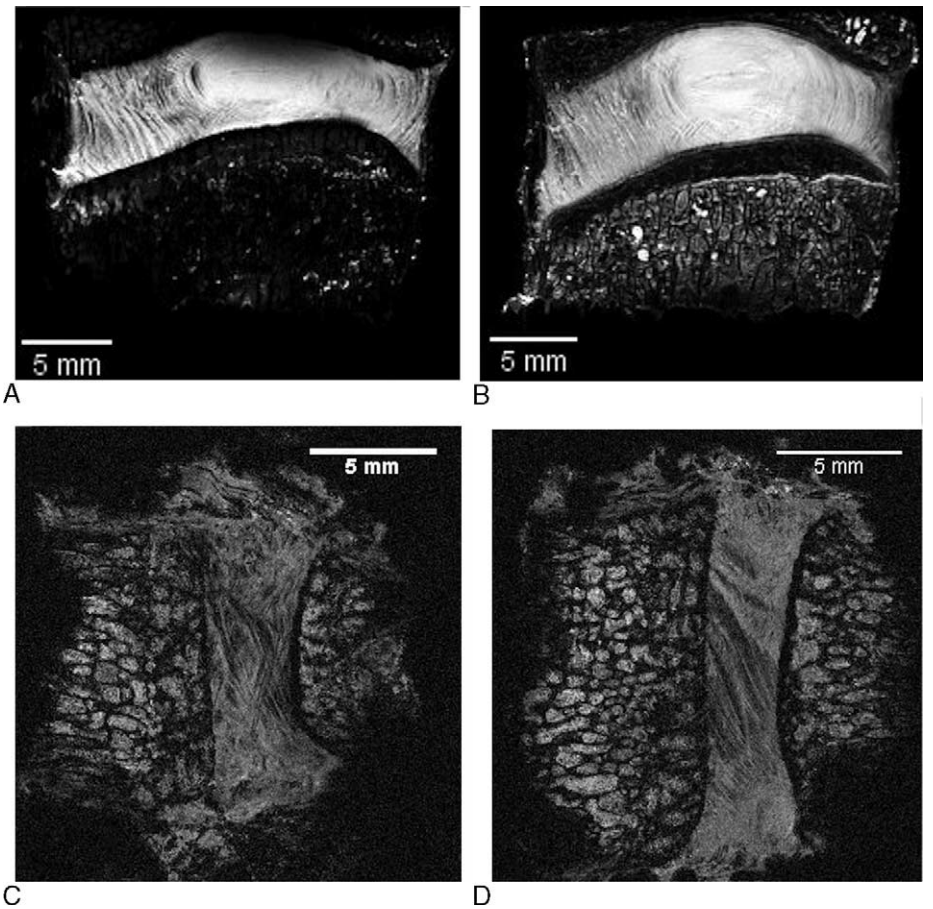

Figure 4. (**A**) Selected slice from the C7–T1 disc predecalcification, MSME sequence. (**B**) Selected slice from the C7–T1 disc post decalcification, MSME sequence (Supplemental Digital Content 1–10, available at: http://links.lww.com/BRS/B20 show additional images for the C7–T1 disc postdecalcification). (**C**, **D**) Selected slices from the T2–T3 disc, Flash sequence. (Supplemental Digital Content 11–20, available at: http://links.lww.com/BRS/B21 show additional images for the T2–T3 disc).

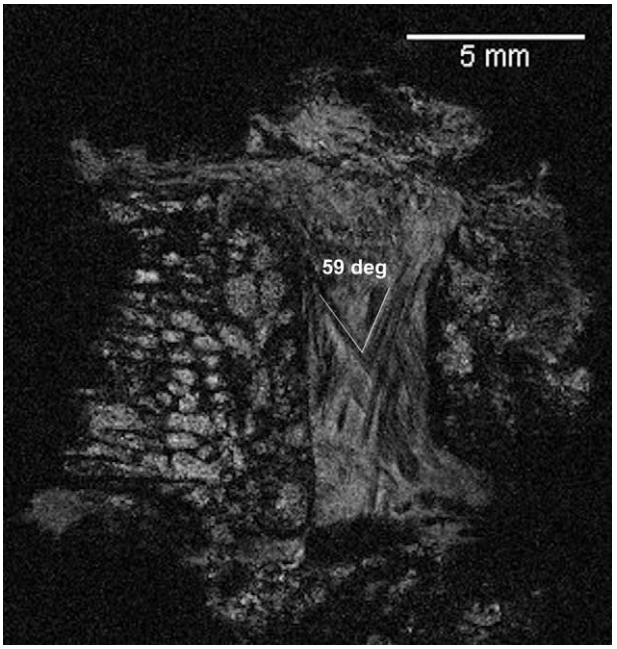

Figure 5. GE (FLASH) image located at the anterior margins of the T2–T3 IVD, demonstrating fiber angle measurement.

micrographs that lamellae thicknesses vary considerably (Figure 2). MR and histology images matched well in terms of the lamellae number, shape, position and orientation. However, due to the relatively low number of voxels across each lamella, attempts were not made in this study to measure the thickness of the lamellae. As such, on the MRI images, peaks and troughs of the grayscale profile along a selected length were used only to interpret the lamellae alternation (Figure 3).

The lamellae architecture demonstrated here, especially the fiber alternating pattern, is not visible *in vivo* using routine MR imaging pulse sequence protocols and may be impossible to visualize even when using specially optimized imaging protocols in a high field (3T) clinical system. This alternating pattern is also difficult to visualize using normal 2D histological techniques across the whole disc, due to its 3D morphology. The identification of the lamellae structure across the entire AF, the lamellae discontinuities and the visualization of fiber bundles in the AF were only possible due to the higher spatial resolution adopted in the study. Furthermore it facilitated clearer demarcation of the main IVD regions; the AF, NP and the EP. The technique presented here therefore exhibits the potential for improved 3D structural characterization. It has important applications in computer-aided simulation of tissue structures because better definition of morphology during model development certainly increases the accuracy of the simulation outcomes.

There are also potential applications in minimally invasive procedures and microsurgery, where detailed preparation and surgical planning with the aid of high resolution and 3-dimensionally reconstructed MRI data would help individually tailored, safe and precise surgical approaches.

Disc degeneration is associated with biochemical and morphological changes. Previously, planar morphological IVD measures (height, width, and shape) have been studied in the context of IVD degeneration and ageing, to understand the symptoms and factors influencing the lower back pain.[17] It is thought that disc injuries such as needle punctures, annular tears or ruptures, contribute toward disc degeneration in the longer term. IVD herniation is a major cause of back pain but the underlying mechanisms are still not well understood. Based on animal studies Tampier *et al*[18] has suggested that formation of clefts in weaker areas in lamellae due to intradiscal pressure, and the nucleus material advancing through these clefts toward the periphery. Prime sites for these weaker areas are where lamellae discontinuities exist or lamellae thickness narrows. High resolution 3D volumetric data sets allow improved recognition of any advancement of nuclear material through these sites, thereby facilitating early detection of prospective disc herniation.

Adverse spinal loading is thought be a key driver for early disc degeneration. Although there are studies that outline measurement of regional strains, mostly under axial loading, a matter that is under considerable discussion is the lamellae deformation pattern, particularly the inner layers, at various locations, under different modes of loading (*e.g.*, flexion, extension). Here again, the positive results of this study demonstrate the potential of high resolution 3D data sets to expand the current understanding.

This study has highlighted the potential of ultrahigh-field strength MRI to obtain higher quality 3D volumetric MRI datasets for better structural characterization. The extra-long acquisition times seen here pose a major limitation and a challenge for clinical translation of the method.

TABLE 5. Quantitative Comparison of Selected MRI Slices With Correspondingly Located Histology Micrographs (Values Rounded off to a Single Decimal Place)

Proportional Distance From Disc Lateral Margin	Disc Height at the Midline (mm)		Bony Endplate Thickness at the Midline (mm)		Major Lamellae Section Counts		Matching Land Marks
	MRI	Histo	MRI	Histo	MRI	Histo	
0.2	6.7	6.4	1.7	1.7	6	6	Yes
0.4	7.3	6.6	2.0	1.9	22	23	Yes
0.6	7.3	7.2	1.9	1.9	22	22	Yes
0.8	6.8	6.7	1.9	1.8	14	18	Yes

However, the technical development of MRI is still continuing and improvements in hardware and detector systems are paving the way for more efficient image acquisition. Recent technical and methodological developments such as parallel MRI techniques[19] and advances in signal processing[20] are resulting significantly reduced acquisition times and have potentially opened new avenues for the clinical application of ultrahigh-field MRI. It is possible that the acquisition time could be reduced by increasing the echo train length. Further work is needed to investigate whether it is possible to identify the IVD lamellae architecture *in vitro* through optimization of pulse sequences to obtain sufficient spatial resolution in a clinical 3T MR system. If so, the findings could be compared with larger scale MR imaging methods which may enable characterization of the IVD and could potentially be translated to *in vivo* imaging.

In summary, the positive results of this study demonstrate the prospects of ultrahigh-field strength MR to nondestructively characterize the 3D structure of the IVD. This has applications in preclinical testing, for example in imaging *in vitro* specimens before and after simulated interventions or loading regimes to examine changes in substructure. In the longer term, if higher field strength systems become more widespread clinically, then their capacity to visualize the disc substructure mean they have the potential to become an important diagnostic tool.

➢ Key Points

- ❑ The use of ultrahigh-field (4—11 T) MRI for spinal applications has been relatively limited.
- ❑ In this study, ovine spinal segments containing the IVDs were successfully imaged using 3D SE MSME (multislice-multiecho) pulse sequence and 3D GE Fast Low-Angle Shot (FLASH) pulse sequence.
- ❑ In comparison with the outcome of the GE FLASH sequence, the SE MSME sequence exhibited higher SNR but with a longer acquisition time.
- ❑ The images revealed greater details on the substructure of the IVDs including the alternating fiber arrangement in the AF which is extremely difficult to capture nondestructively.

Supplemental digital content is available for this article. Direct URL citations appearing in the printed text are provided in the HTML and PDF version of this article on the journal's Web site (www.spinejournal.com).

References

1. Macfarlane GJ, Thomas E, Croft PR, et al. Predictors of early improvement in low back pain amongst consulters to general practice: the influence of premorbid and episode-related factors. *Pain* 1999;80:113–9.
2. Freemont AJ, Watkins A, Le Maitre C, et al. Current understanding of cellular and molecular events in intervertebral disc degeneration: implications for therapy. *J Pathol* 2002;196:374–9.
3. Roberts S, Evans H, Trivedi J, et al. Histology and pathology of the human intervertebral disc. *J Bone Joint Surg Am* 2006;88 (Suppl 2):10–4.
4. Bernstein MA, Huston J, Ward HA. Imaging artefacts at 3.OT. *J Magn Reson Imaging* 2006;24:735–46.
5. Gutberlet M, Noeske R, Schwinge K, et al. Comprehensive cardiac magnetic resonance imaging at 3.0 tesla — feasibility and implications for clinical applications. *Invest Radiol* 2006;41:154–67.
6. Schindera ST, Miller CM, Ho LM, et al. Magnetic resonance (MR) cholangiography—Quantitative and qualitative comparison of 3.0 Tesla with 1. *5 Tesla Invest Radiol* 2007;42:399–405.
7. Schmidt GP, Wintersperger B, Graser A, et al. High-resolution whole-body magnetic resonance imaging applications at 1.5 and 3 Tesla—A comparative study. *Invest Radiol* 2007;42:449–59.
8. Kuo R, Panchal M, Tanenbaum L, et al. 3.0 Tesla imaging of the musculoskeletal system. *J Magn Reson Imaging* 2007;25:245–61.
9. Neubert A, Fripp J, Engstrom C, et al. Automated detection, 3D segmentation and analysis of high resolution spine MR images using statistical shape models. *Phys Med Biol* 2012;57 (24):8357–76.
10. Kaufman L, Kramer DM, Crooks LE, et al. Measuring signal-to-noise ratios in MR imaging. *Radiology* 1989;173:265–7.
11. Henkelman RM. Measurement of signal intensities in the presence of noise in MR images. *Med Phys* 1985;12:232–3.
12. Lavdas E, Vlychou M, Arikidis N, et al. Comparison of T1-weighted fast spin-echo and T1-weighted fluid-attenuated inversion recovery images of the lumbar spine at 3.0 Tesla. *Acta Radiol* 2010;3:290–5.
13. Li X, Huang W, Rooney WD, et al. *QIN Signal-to-noise ratio, contrast-to-noise ratio, and pharmacokinetic modelling considerations in dynamic-contrast-enhanced magnetic resonance imaging Magn Reson Imaging* 2012;30:1313–22.
14. Bancroft JD, Gamble M. Theory and Practice of Histological Techniques. 5th ed. Churchill Livingstone; 2002.
15. Roemer PB, Edelstein WA, Hayes CE, et al. The NMR phased array. *Magn Reson Med* 1990;16:192–225.
16. Bydder GM. New approaches to magnetic resonance imaging of intervertebral discs, tendons, ligaments and menisci. *Spine* 2002; 27:1264–8.
17. Pfirrmann CW, Metzdorf A, Elfering A, et al. Effect of aging and degeneration on disc volume and shape: a quantitative study in asymptomatic volunteers. *J Orthop Res* 2006;24:1086–94.
18. Tampier C, Drake JDM, Callaghan JP, et al. Progressive disc herniation, an investigation of the mechanism using radiologic, histochemical, and microscopic dissection techniques on a porcine model. *Spine* 2007;32:2869–74.
19. Deshmane A, Gulani V, Griswold MA, et al. Parallel MR imaging. *J Magn Reson Imaging* 2012;36:55–72.
20. Lustig M, Donoho D, Pauly JM. Sparse MRI: the application of compressed sensing for rapid MR imaging. *Magn Reson Med* 2007;58:1182–95.